



22 thermophiles and solved by crystallography. In the presence of the nucleotide mixture, BfpD  
23 bound exclusively AMP-PNP and this binding resulted in a modest outward expansion in  
24 comparison to the structure in the presence of ADP, suggesting a concerted model for hydrolysis.  
25 *De novo* molecular models reveal a partially open configuration of all subunits where the  
26 nucleotide binding site may not be optimally positioned for catalysis. ATPase functional studies  
27 reveal modest activity similar to that of other extension ATPases, while calculations indicate that  
28 this activity is insufficient to power pilus extension. Our results reveal that, despite similarities in  
29 primary sequence and tertiary structure, T4P extension ATPases exhibit divergent quaternary  
30 configurations. Our data raise new possibilities regarding the mechanism by which T4P extension  
31 ATPases power pilus formation.

32

33

## 34 INTRODUCTION

35 Type 4 pili (T4P) are the most ancient and widespread class of pili, produced by Gram-positive  
36 and Gram-negative bacteria and by archaea (1). T4P are composed of thousands of copies of a  
37 major pilin protein arranged in a helical array (2). They are assembled and retracted by a complex  
38 machine composed of several essential proteins, including a dedicated extension ATPase most  
39 often called PilB that is essential for pilus biogenesis. Prior to incorporation into the pilus, pilin is  
40 an integral transmembrane protein (3). Thus, PilB is thought to provide mechanical energy  
41 required to extricate the pilin from the cytoplasmic membrane to assemble the pilus. The enzyme  
42 activities of several purified T4P extension ATPases have been measured *in vitro*, with reported  
43 rates varying from 0.7 to 700 nanomoles of ATP hydrolyzed per minute per mg protein (4-9). How  
44 this *in vitro* activity relates to pilus extension, which has been measured in microns per second  
45 (10-12), remains unclear. Many bacteria also have one or more dedicated retraction ATPases (4,  
46 10, 12, 13).

47 Precisely how conformational changes induced by ATP hydrolysis are transduced by PilB to lift  
48 and extricate pilin from the membrane so that it can be added to the base of the growing pilus  
49 remains an unanswered question (14). High-resolution structures of catalytic domains of three  
50 closely related PilB-family ATPases solved by X-ray crystallography revealed a two-fold symmetry  
51 of the hexamers (14-17), whereas other members of the AAA+ family of ATPases display six-fold  
52 symmetry (18-20). The PilB structures, all from thermophilic Gram-negative bacteria, have several  
53 other features in common: (1) all are hexamers; (2) the first N-terminal domain (N1D) is not  
54 visualized; (3) a flexible linker separates the second N-terminal domain (N2D) from the C-terminal  
55 domain (CTD), which contains the catalytic site; (4), a density is consistent with a Mg<sup>2+</sup> ion and  
56 (5) remote from the active site, is a zinc-binding motif. Within each structure are three pairs of

57 subunits on opposite sides of the hexamer. In one pair, relative to the other two, the N2D is rotated  
58 towards the center of the toroid (NTD-in), while in the other two pairs the N2D is rotated away  
59 from the center (NTD-out). A symmetric, rotatory mechanism of hydrolysis has been proposed,  
60 which results in a “scooping” motion in which the CTD is displaced upward and toward the center  
61 of the ring, where it could translate this motion to membrane-bound pilin (14, 15).

62 PilB from *Thermus thermophilus* (TtPilB) was also examined by cryo-EM, both bound to the non-  
63 hydrolysable ATP analogue adenylyl-imidodiphosphate (AMP-PNP) and without exogenous  
64 nucleotide. Although resolution of only  $\sim 8$  Å was achieved, this structure showed for the first time  
65 the second and third of three predicted N1Ds (16). This more complete structure showed two  
66 hexamers joined by a constriction. One of the hexamers, into which the N2D-CTD crystal structure  
67 was docked, showed clear two-fold symmetry. The other hexamer, presumably representing the  
68 second and third N1Ds, appeared to display six-fold rather than two-fold symmetry. Comparison  
69 of the hexamers in the presence of AMP-PNP and without added nucleotide showed little  
70 evidence for the symmetric rotary model, nor for translation of movement through the center of  
71 the multimer. Instead, cryo-EM shows an outward shift in the center of mass of the AMP-PNP  
72 structure relative to the structure solved without addition of nucleotide, rather than the change in  
73 the orientation of the N2D-CTD protomers seen by crystallography (14, 15). Evidence of  
74 displacement of the N1D hexamer by 10-13 Å was also reported. The authors suggested an  
75 alternative model linking the N1D displacement to pilin extrication.

76 Overall, while available PilB structures have provided valuable information, there is no agreement  
77 yet on the significance of the two-fold symmetry, whether it is critical to explain the mechanism  
78 by which chemical energy is converted to mechanical energy, and which structural changes are  
79 caused by ATP hydrolysis.

80 Here, we focused on the extension ATPase from a Gram-negative human pathogen,  
81 enteropathogenic *Escherichia coli* (EPEC), which expresses a bundle-forming pilus (BFP)  
82 distantly related to T4P of thermophiles (21). We purified the full-length EPEC PilB homologue,  
83 BfpD, determined its structure by cryo-EM both in the presence of ADP alone and in the presence  
84 of a mixture of ADP, ATP, and AMP-PNP, achieving unprecedented resolutions of 3.0 and 3.1 Å,  
85 respectively, and measured its enzyme activity. The six-fold symmetry that we observed suggests  
86 a concerted, rather than a symmetric rotary mechanism of energy coupling that may have  
87 implications relevant to all PilB family members.

88

## 89 **RESULTS**

90

### 91 **Negative staining and cryo-EM of BfpD reveal a six-fold symmetry**

92 Purified BfpD was prepared under two nucleotide conditions: either in the presence of ADP (BfpD-  
93 ADP dataset), or in the presence of ADP, ATP and the non-hydrolysable ATP analog, AMP-PNP  
94 (termed BfpD-ANP dataset) at a ratio of 2:4:5. We reasoned that the presence of ATP would allow  
95 completion of catalysis culminating in occupancy by the nucleotide preferred by each subunit,  
96 depending on its position in the catalytic cycle. Examination of BfpD-ANP by negative staining in  
97 the presence of a reducing agent showed the expected toroid structure, and further reference-  
98 free alignment showed 2D averages with six-fold symmetry with protruding edges (Fig. S1).

99 After confirming structural integrity of the sample, cryo-EM and high throughput data collection  
100 yielded 7,207 good movies and 313,223 good particles for BfpD-ADP. For BfpD-ANP, a dataset  
101 of 9,853 good movies and 424,708 good particles with well-distributed orientation yielded two  
102 classes, with 214,673 and 58,944 particles, respectively. Reference-free 2D averaging

103 demonstrates unambiguous six-fold symmetry in both nucleotide states (Fig. S2-S3). Subsequent  
104 3D reconstruction with C6 symmetry yielded resolutions of 3.1 Å, 3.0 Å and 3.7 Å for BfpD-ADP,  
105 BfpD-ANP class-1 and BfpD-ANP class-2, respectively (Figs.1, S2-S3). BfpD-ANP class-1 has  
106 an outward N2D compared to BfpD-ANP class-2. The dimensions of BfpD are 130 Å maximum  
107 width, 68 Å height, with a central pore measuring 30 Å in diameter on one side and twice this  
108 diameter on the other.

109

### 110 **Overall BfpD structure, active site, and hexameric association**

111 *De novo* models were built for residues 107-219, which represents the N2D and 232-534, which  
112 represents the CTD (Fig. 2A, B). N1D and the eight residues intervening the two domains were  
113 not visualized, probably owing to intrinsic flexibility, as has been reported for other T4P extension  
114 ATPases (14-17). The catalytic site is formed by the interface between the Arginine finger (Arg  
115 217) of N2D, the Walker A motif (260-267), and the catalytic loop of the CTD (294-310) of each  
116 subunit (Figs 2-3). For the BfpD-ANP dataset, despite the addition of ADP, ATP, and AMP-PNP,  
117 the active site of all monomers was fully occupied by electron density consistent with AMP-PNP,  
118 suggesting that ultimately ANP occupied the active sites and remained there. The presence of  
119 ANP in the catalytic site results in an outward N2D movement, stabilized by interaction between  
120 Arg 217 and the  $\gamma$ -phosphate. Both structures show catalytic glutamate residue Glu295 and  
121 Walker B motif Glu338, 5.3-11.6 Å and 6 Å, respectively, from the phosphorus atom in the terminal  
122 nucleotide phosphate (Figs. 2, 3). The loop (294-310) carrying the catalytic Glu295 has a well-  
123 defined cryo-EM density and is positioned closer to the nucleotide in BfpD-ADP compared to  
124 BfpD-ANP, assisted by a hydrogen bond between ADP and Tyr296 (Figs. 2, 3). Additionally, in  
125 the BfpD-ADP map,  $Mg^{2+}$  is seen between Ser267 (from the Walker A motif) and the beta-  
126 phosphate of ADP. As in other PilB-family members,  $Zn^{2+}$  is observed far from the catalytic site

127 and from the subunit interface (Fig. 2B), coordinated by the zinc-finger-like tetracysteine motif  
128 (Cys403, Cys406, Cys445, Cys446).

129 The electrostatic map shows the toroid surface lined by the N2D domains as the side that likely  
130 faces the membrane, because, in comparison to the CTD side, its positive charge density is  
131 significantly higher (Fig. 4 A, B). Each subunit forms a chevron-like structure pointing to the right  
132 (+ subunit) when seen sideways with the N2D on top (Figs. 1, 4C). At the inter-subunit interface,  
133 the outer corner of the chevron, formed by the CTD, points towards the inner corner of the  
134 neighboring (+) subunit, interacting by the N2D/CTD and CTD/CTD+ interfaces, with  $\sim 1400 \text{ \AA}^2$   
135 buried surface area. The ATP binding site is not involved in the inter-subunit interaction. Several  
136 residues face each other within  $3.8 \text{ \AA}$ , suggesting potential salt bridges or hydrogen bonds  
137 between adjacent subunits. Starting from the N' terminus of the subunit in the left, the pairs of  
138 residues likely forming hydrogen bonds are R328-Q203, N286-Y213, N286-K129, and those likely  
139 forming salt bridges are D330-R140, D332-R140, K383-D376, D386-R475 (Fig. 4C), where the  
140 second residue is from the (+) subunit.

141

## 142 **Presence of trinucleotide induces an expansion in the AAA+ ATPase while preserving the** 143 **six-fold symmetry**

144 Comparison of the BfpD-ADP and BfpD-ANP structures reveals a subtle outward shift in position  
145 of the N2D with respect to the CTD such that the mobile innermost N2D loops delineate a circle  
146 of  $65 \text{ \AA}$  in diameter (distance between diagonally located Ala172 residues) in the presence of  
147 ADP, and  $70\text{-}73 \text{ \AA}$  diameter in the presence of ANP class 1 and 2, respectively (Fig. 1). This  
148 change is accompanied by a slight change in angle of  $1.1^\circ$  for the N2D and  $1.6^\circ$  for the CTD  
149 between each monomer and the vertical axis for the BfpD-ANP structure compared to the BfpD-  
150 ADP structure (Movie S1), which is consistent with the outward shift in the center of mass

151 described in the much lower resolution TtPilB cryo-EM structure (16). The conservation of six-fold  
152 symmetry in both BfpD structures suggests that the subunits may work in a concerted manner to  
153 translate chemical to mechanical energy.

#### 154 **The N2D-CTD domains of BfpD have an intermediate rotation state**

155 We compared BfpD with the four other T4P extension ATPases homologues, each of which has  
156 two-fold symmetry, to try to understand the mechanistic basis of force generation.

157 The TtPilB-ATP $\gamma$ S crystal structure (PDB ID:5IT5) is an elongated hexamer with two-fold  
158 symmetry (15). In TtPilB, all six subunits are bound to ATP $\gamma$ S. However, one pair of opposing  
159 subunits in the hexameric ring is in the N2D-in, or “closed” conformation, and the other four  
160 subunits are in the N2D-out “open” conformation. The four open N2D-out subunits are  
161 superimposable, as are the two closed N2D-in subunits (Fig. 5A). With the C-terminal domains  
162 superimposed, we found that the open subunits have a 57° outward rotation of their N2D domain,  
163 *i.e.*, away from the center of the toroid (N2D-out), when compared to the closed subunits (Fig.  
164 5A). Comparing BfpD-ANP to TtPilB-ATP indicated an intermediate conformation: the BfpD N2D  
165 is rotated by ~42° from the TtPilB closed conformation and 18° from the TtPilB open conformation  
166 (Fig. 5B). Similar results were obtained for BfpD-ADP, as the rotation of N2D between the two  
167 nucleotide states was ~1°.

168 The *Geobacter metallireducens* PilB (GmPilB)-ANP and GmPilB-ADP crystal structures are also  
169 two-fold symmetric hexamers, wherein four subunits are bound to ANP or ADP, respectively (14).  
170 The other two subunits in GmPilB-ANP and GmPilB-ADP structures bind to ADP and are empty,  
171 respectively. Two fully closed (N2D-in), two fully open (N2D-out), and two open intermediate  
172 subunits were found in GmPilB-ANP (PDB ID: 5TSH). Within each of the three pairs, the two  
173 subunits are superimposable (Fig. S4). The fully open pair of subunits are rotated ~60° in their  
174 N2D from the closed subunits. However, the N2Ds of the intermediate-open subunits are rotated



175 by 11° inward from the fully open subunits or rotated by 49° from the closed pair of subunits. BfpD-  
176 ANP showed ~46° rotation in its N2D domain from the GmPilB-ANP closed subunits. Consistent  
177 with the three distinct kinds of subunits, the nucleotide-binding pockets of GmPilB at the N2D-  
178 CTD domain interfaces have different occupancy by ATP and thus varied affinity to the nucleotide.  
179 The N2D-in subunits have 100% occupancy of ANP and are proposed to be the active ATP  
180 hydrolysis interface. The catalytic Glu395 at this interface is located closest (at ~6 Å) from the  
181 phosphorous atom of the ANP terminal phosphate. The other two pairs of subunits with ANP and  
182 ADP form an open and closed ATP binding pockets with N2D twists and 0° and 49° respectively  
183 and partial occupancy of 58-60% ANP and 44-54 % ADP, respectively. Larger  $\gamma$ -P distances of  
184 terminal phosphates, ~10 Å at the ADP and 7-8 Å at the ANP interface, are suggestive of ATP  
185 binding and ADP/ATP exchange sites.

186 Furthermore, the *G. sulfurreducens* PilB (GsPilB) apo structure (PDB ID: 5ZFR) was also found  
187 to possess three distinct N2D conformations (17). Two pairs of the open N2D subunits have 66°  
188 and 59° rotations from the closed (N2D-in) pair of subunits (Fig. 5A). BfpD-ANP showed a ~42°  
189 rotation in its N2D domain from the GsPilB-ANP closed subunits (not shown).

190 The moderate twist of the N2D domain in the BfpD structure is suggestive of a partially open  
191 conformation. The N2D twist is similar to that of the pair of subunits in the GmPilB-ANP structure  
192 with a N2D twist of 48°, nevertheless with a distinct rotation axis. As Glu338 and the catalytic  
193 glutamate Glu295 are 5.3-11.6 Å away from the  $\gamma$ -phosphate of ANP, it appears that the ATPase  
194 captured by cryo-EM is a pre-hydrolysis intermediate between the ADP/ATP exchange and ATP  
195 hydrolysis steps of the catalysis cycle. The single rotation state of the N2D domain with respect  
196 to the CTD in the case of BfpD concurs with its six-fold symmetry.

197

198 **Insertions in the BfpD sequence might account for its six-fold symmetry**

199

200 Amino acid sequences from five type-4 pilus extension ATPase homologues, including three that  
201 form two-fold symmetric structures and two from pathogens that have extension ATPases closely  
202 related to those of the thermophiles, were compared with BfpD. BfpD showed conservation in the  
203 catalytic glutamate, Walker A/B motifs and arginine fingers which are required for nucleotide  
204 binding, stability and hydrolysis (Fig. 6). However, several insertions were observed when the  
205 N2D and CTD were aligned separately. The N2D contains four conserved arginines, two of which  
206 are bound by ATP in the pair of active hydrolyzing subunits in TtPilB (PDB ID: 5IT5). We observed  
207 insertions in BfpD around Arg183, Arg217, the linker, and in the catalytic loop that harbors the  
208 critical catalytic residue, Glu295 (Fig. 6). We hypothesize that a longer linker and a shift in  
209 arginine fingers might be responsible for a different N2D twist seen in BfpD. Furthermore, half of  
210 the inter-subunit contacts in BfpD-ANP and BfpD-ADP structures were not conserved among its  
211 two-fold symmetric homologues. Taken together, the above sequence differences in the linker  
212 and oligomerization interface might be implicated in the observed six-fold symmetry in BfpD.

213

214

215

### 216 **BfpD ATPase activity and kinetics**

217

218 According to molecular modeling with another AAA+-family ATPase (22), the putative catalytic  
219 E295 residue in our cryo-EM BfpD model seems to be positioned further from the nucleotide than  
220 required for catalysis (Fig. 3 and Movie S2). We therefore examined BfpD activity, using enzyme  
221 that had been purified by metal affinity and size exclusion chromatography. We varied the  
222 concentration of ATP in the reaction and determined that the apparent  $V_{max}$  and  $K_m$  of BfpD at 0.5  
223 mg/ml are  $2.69 \pm 0.34 \mu\text{mole min}^{-1}$  and  $239.31 \pm 117.63 \mu\text{M}$ , respectively (Fig. 7A). At an ATP  
224 concentration of 3 mM, the specific activity of BfpD was  $3.16 \pm 0.60 \text{ nmol min}^{-1} \text{ mg}^{-1}$  (Fig 7B),

225 which is consistent with published results for other PilB family extension ATPases (4-7). To  
226 assess the role of residues mapped to the catalytic site, we expressed and purified BfpD variants  
227 that had mutations in the catalytic glutamate (BfpD<sub>E295C</sub>), and in both that residue and the  
228 conserved Walker B glutamate (BfpD<sub>E295C E338Q</sub>). The single and double glutamate mutations  
229 reduced the catalytic rate by 5- and 12-fold, supporting their important role in ATP catalysis.  
230 However, in each case, we were able to measure specific activity above background spontaneous  
231 hydrolysis (Fig 7A). The specific activity of BfpD<sub>E295C</sub> was  $0.69 \pm 0.28$  nmol min<sup>-1</sup> mg<sup>-1</sup> and that of  
232 BfpD<sub>E295C E338Q</sub> was  $0.38 \pm 0.10$  nmol min<sup>-1</sup> mg<sup>-1</sup>. Importantly, while a plasmid encoding wild type  
233 BfpD was able to complement a *bfpD* null mutant to restore bacterial auto-aggregation  
234 characteristic of EPEC expressing BFP, plasmids encoding either the E295C or the E338Q BfpD  
235 variants were not (Fig. 7C). Thus, the residual activity we were able to detect is insufficient for  
236 function.

237

## 238 **DISCUSSION**

239 Using cryo-EM, we determined the structure of BfpD, the extension ATPase of the EPEC bundle-  
240 forming T4P. The structure is noteworthy for a number of reasons. It is the first near-atomic  
241 structure of a T4P PilB homologue in its native, frozen-hydrated state. It is the first such structure  
242 from a pathogenic bacterium. It is an enzyme that is distantly related to its homologues solved to  
243 date, all of which were from thermophiles (14). Despite its phylogenetic distance, the BfpD  
244 monomer is similar to those of other PilB structures (14-17). As has been the case with all PilB  
245 structures solved to date, the full BfpD N-terminus (N1D) was not visualized. In addition, the eight  
246 residues intervening the N2D and CTD domains, where flexible linkers exist in the PilB structures,  
247 were not resolved here. BfpD was determined either in the presence of ADP or ADP plus ANP.  
248 In the BfpD-ANP reconstruction, despite the presence of ADP, ATP and ANP, the six nucleotide  
249 binding sites were occupied by the triphosphate or its analogue. Transition from BfpD-ADP to

250 BfpD-ANP resulted in a slight outward shift of the top part of the toroid, a tendency more  
251 pronounced in BfpD-ANP class 2. A similar conformational transition was observed by lower-  
252 resolution cryo-EM for the TtPilB-ANP structure relative to the structure purified without nucleotide  
253 (14, 15). The BfpD monomers are in a nearly identical conformation in both cases. The isolated  
254 N2D and CTD domains of BfpD superimpose well with those determined for other PilB structures,  
255 while the relative N2D-CTD position is intermediate between the two more extreme open and  
256 closed conformations manifested by the other PilB structures.

257 In contrast to the similarity among monomers of PilB structures, the BfpD quaternary structure  
258 revealed unambiguous six-fold symmetry, while those of the PilB enzymes from thermophilic  
259 bacteria show two-fold symmetry. The two-fold symmetry is the basis for a symmetric rotary model  
260 coupling ATP hydrolysis to large domain shifts, proposed to be translated via the conserved  
261 polytopic membrane protein, PilC in the center of the toroid, to lift pilin from the membrane (14,  
262 15). In contrast, a six-fold symmetry is more compatible with a concerted model, in which all  
263 catalytic sites act synchronously. Of note, the crystal structure of a catalytically inert C-terminal  
264 proteolytic fragment of TtPilB containing the N2D and CTD also displayed two-fold symmetry (16),  
265 as does the crystal structure of the N2D-CTD fragment of GsPilB, which was solved in its apo  
266 form (17). Thus, ATP hydrolysis is not required for the two-fold symmetry.

267 TtPilB was also examined by cryo-EM, both bound to AMP-PNP and without exogenous  
268 nucleotide, achieving resolution of only  $\sim 8$  Å, but, for the first time, the second and third of three  
269 predicted N1Ds were observed (16). Comparison of the hexamers in the presence of AMP-PNP  
270 and without added nucleotide showed an outward shift in the center of mass of the AMP-PNP  
271 structure relative to the structure purified without addition of nucleotide (14, 15). They also  
272 observed evidence of displacement of the N1D hexamer by 10-13 Å and suggested an alternative  
273 model for energy transduction in which the N1D displacement is linked to pilin through a  
274 transmembrane complex of essential T4P biogenesis proteins called PilM, PilN, PilO, and PilP.

275 The BfpD structures in the presence of ADP and AMP-PNP, while not compatible with the  
276 symmetric rotary model, show subtle differences in the position of the N2D with respect to the  
277 CTD that are similar to those seen in the TtPilB cryo-EM structures (16). These shifts may  
278 represent evidence for transduction of mechanical energy at the periphery of the toroid, rather  
279 than through PilC at its center. Given that structures of the N1Ds of T4P ATPases have yet to be  
280 solved, it is possible that these differences are amplified by conformational changes and  
281 transmitted through PilM and PilN to the outer surface of the cytoplasmic membrane. Support for  
282 this alternative model is found in the structure of the related type 2 secretion ATPase N1D in  
283 complex with the PilM homologue (23) and in the complex formed by a T4P pilin with the PilM,  
284 PilN, PilO transmembrane assembly (24).

285 The conformation of the BfpD nucleotide binding site raises interesting questions about its  
286 catalytic activity, as the distances of the putative catalytic Glu295 and of the conserved Walker B  
287 Glu338 are approximately 5.3-11.6 Å and 6 Å from the phosphorus atom in the ANP  $\gamma$ -phosphate,  
288 respectively. This appears to be too far for activation of the water molecule that is responsible for  
289 hydrolysis (20). By comparison, the corresponding distances of 6-6.5 Å at the tightest interface in  
290 the GmPilB-ANP structure, suggesting that all subunits in the BfpD-ANP structure are in a pre-  
291 hydrolytic conformation. Nevertheless, we were able to demonstrate that BfpD has ATPase  
292 activity that is comparable to that reported for several other such enzymes (4-8). Surprisingly, we  
293 were also able to measure ATPase activity above background in a BfpD variant that has mutations  
294 in both Glu295 and Glu338, which suggests that mere binding of ATP to the open pocket facilitates  
295 hydrolysis. However, the residual activity is insufficient for pilus biogenesis, as demonstrated by  
296 expressing these variants in a *bfpD* null mutant. We further suggest that neither the *in vitro* activity  
297 we were able to measure in wild type BfpD, nor that of any other PilB homologue is sufficient to  
298 power T4P extension. BfpD specific activity of about 3 nmol min<sup>-1</sup> mg<sup>-1</sup> corresponds to 0.02 ATP  
299 molecules hydrolyzed per second per hexamer. In contrast, given an axial rise of 10.5 Å,

300 corresponding to 952 subunits per micron in a T4P (25), real-time video demonstrates that the  
301 rate of T4P extension equates to 333 - 1072 subunits added per second (10-12). Assuming that  
302 each subunit added requires at least one ATP, these *in vitro* enzyme activity measurements fall  
303 short of the values required *in vivo* by more than 10,000-fold. If six ATPs are required per subunit,  
304 this shortfall multiplies correspondingly. Modifications to the *in vitro* assays, such as addition of  
305 phospholipids or partner proteins (26), or imposed hexamerization (27), as well adjustments to  
306 the assumptions, would do little to alter this arithmetic. A similar conclusion was reached by the  
307 authors of the study that described a thermophilic PilB enzyme with specific activity of 700  
308 nanomoles  $\text{mg}^{-1} \text{min}^{-1}$  (9). They suggested that enzyme activity must be higher *in vivo* where  
309 partner proteins are in optimal orientation and concentration. Interestingly, these authors  
310 described complex enzyme kinetics including substrate inhibition at concentrations exceeding 1.5  
311 mM ATP and a non-linear relationship between substrate concentration and catalytic rate below  
312 that concentration. They interpreted these results as consistent with the symmetric rotary model  
313 of catalysis that had been proposed for TtPilB. In contrast, BfpD displayed simple Michaelis-  
314 Menton kinetics compatible with a concerted model. The fact that all enzyme subunits were  
315 occupied by the nucleotide triphosphate or triphosphate analogue in the presence of ADP, ATP,  
316 and ANP is also consistent with a concerted model.

317 In summary, we report the first 3D structure of a T4P extension ATPase from a human pathogen.  
318 The BfpD structure determined under cryogenic conditions in a native state, unparalleled in its  
319 detail, in the presence of ADP and a non-hydrolysable ATP homologue, lays a structural  
320 foundation to understand similarities and differences of T4P machinery among different clades.  
321 The study expands our understanding of mechanisms of catalysis, activation, and energy  
322 transduction of the PilB family of T4P extension ATPases.

323

## 324 **METHODS**

### 325 **Site-directed mutation of putative BfpD active site residues**

326 All bacterial strains and plasmids used in this study are listed in Table S2. A codon-optimized  
327 *bfpD* gene in plasmid BfpD-Hcp (GenScript, USA, a kind gift from Dr. Kurt Piepenbrink, Fig. S5)  
328 was amplified using PCR with primers BfpDNcol and BfpDXhol (Table S3), creating a Leu to Val  
329 substitution at codon two to allow cloning into a pET30a plasmid vector at Ncol/XhoI sites and  
330 creating plasmid pJZM005. FastCloning (28) was used to introduce substitutions for glutamate  
331 codons at amino acid positions 295 and 338 of BfpD in plasmids pJZM005 and pJZM032,  
332 respectively. In short, a pair of primers (Table S3) was designed such that each has a  
333 complementary sequence including the mutated codon and divergent sequences overlapping with  
334 *bfpD*. Codons specifying neutrally charged hydrophilic amino acids of similar size to glutamate  
335 were chosen to minimize disruptions to structure and those that could be expressed and purified  
336 were studied further. The PCR products were digested with DpnI and subsequently transformed  
337 into *E. coli* DH5 $\alpha$  competent cells. The plasmids pJZM032 and pJZM042 encoding BfpD<sub>E295C</sub> and  
338 BfpD<sub>E295C E338Q</sub> respectively, were confirmed by sequencing, expressed, and purified from *E. coli*  
339 BL21(DE3) as described below. To make plasmids for *in vivo* complementation, we first  
340 constructed a plasmid harboring wild type *bfpD* in low-copy-number cloning vector pWKS30 (29).  
341 To do this, *bfpD* with its N-terminal His tag and S tag, was isolated from pRPA405 (30) as an  
342 XbaI-SacI fragment, and inserted into pWKS30. The resultant plasmid pEMM1 was later  
343 discovered to lack its native stop codon, while a stop codon on the vector was noted downstream,  
344 thus adding an elongated non-native C-terminus to the predicted protein. We used FastCloning  
345 to restore a TAG stop codon in its original position in pEMM1, and the new plasmid was named  
346 pJZM031. Thereafter, pJZM031 was used as template to introduce E295C and E338Q mutations  
347 to obtain pJZM032 and pJZM036, respectively. FastCloning was used to introduce the E295C  
348 mutation. For the E338Q mutation, we first introduced the mutation using overlap extension PCR

349 (31), which was later cloned into pJZM031 (XbaI/SacI digested). Auto-aggregation and  
350 disaggregation were assessed as previously described (30). Briefly, overnight cultures of  
351 E2348/69, UMD926 and VCU019 containing pWKS30, pJZM031, pJZM032, or pJZM036 were  
352 diluted 100-fold in Dulbecco's modified Eagle's medium (Corning) and grown for 4 h at 37 °C  
353 before examination by phase-contrast microscopy.

354

### 355 **BfpD, BfpD<sub>E295C</sub> and BfpD<sub>E295C E338Q</sub> expression and purification**

356 For purification of BfpD, *E. coli* strain BL21(DE3) pJZM005 was grown at 37°C in Luria-Bertani  
357 medium to an optical density at 600 nm (OD<sub>600</sub>) of 0.6 and induced with 1 mM isopropyl β-D-1-  
358 thiogalactopyranoside (IPTG) at 16°C overnight. Cells were harvested by centrifugation,  
359 sonicated in lysis buffer (50 mM PO<sub>4</sub>, 300 mM NaCl, pH 8.0, 10 mM imidazole), and purified by  
360 affinity chromatography on Cobalt-NTA resin, created by stripping nickel from a Ni-NTA (Qiagen,  
361 USA) column with 100 mM EDTA and replacing with 10 mM CoCl<sub>2</sub>. Fractions eluted with 250 mM  
362 imidazole were analyzed by SDS page, combined, and dialyzed against buffer (20 mM Tris-HCl,  
363 pH 7.6, 100 mM NaCl, 1 mM MgCl<sub>2</sub>, 2 mM DTT) at 4°C. For some experiments, a Suprose6 10/300  
364 column was used to achieve further purification, as noted.

### 365 **Negative staining and 2D averaging**

366 BfpD in 20 mM Tris (pH 7.6), 0.1 M NaCl, 5 mM MgCl<sub>2</sub>, 2 mM DTT and 1 mM ADP was diluted to  
367 0.01-0.03 mg/ml and stained with 0.75% uranyl nitrate using an established protocol (32). Images  
368 were acquired at 50000X magnification in low dose mode with a Tecnai F20 microscope operated  
369 at 120kV. Reference-free 2D averages were obtained with the SPIDER program (33).

### 370 **Cryo-EM grid preparation and data acquisition**



371 The cryo-EM sample buffer consisted of 20 mM Tris (pH 7.6), 0.1 mM NaCl, 5 mM MgCl<sub>2</sub>, 2mM  
372 DTT and 0.5 mM CHAPSO, and additionally either a mixture of ADP (1 mM), ATP and ANP at a  
373 2:4:5 millimolar ratio or 1 mM ADP alone. Usage of CHAPSO improved BfpD orientation in  
374 vitreous ice which enabled successful 3D reconstruction. The 300 mesh UltraAufoil -1.2/1.3 holey-  
375 gold (Quantifoil, Germany) grids were cleaned with a customized protocol (34) prior to glow  
376 discharge. Purified BfpD was diluted to 4.5 mg/ml and 3  $\mu$ l was applied to a glow-discharged 300  
377 mesh UltraAufoil -1.2/1.3 holey-gold (Quantifoil, Germany). Grids were blotted for 2 s with ash-  
378 free Whatman<sup>®</sup> Grade 540 filter paper in a Vitrobot Mark IV (ThermoFisher Scientific) and plunged  
379 into liquid ethane. Sample quality and distribution was assessed on a Tecnai F20 (ThermoFisher  
380 Scientific) electron microscope. Data acquisition was carried out in a Titan Krios transmission  
381 electron microscope (ThermoFisher Scientific) operated at 300 kV and counting mode, with a  
382 Gatan K3 detector and a 10 eV slit width Gatan Quantum Energy Filter (GIF). Datasets were  
383 collected in automated mode with the program Latitude (Gatan) with cumulative electron dose of  
384 60 e-/Å<sup>2</sup> applied over 40 frames.

### 385 **Single-particle image processing**

386 Movie stacks collected for BfpD-ANP and BfpD-ADP datasets were processed in cryosparc2.15.  
387 Gain-normalization, movie-frame alignment, dose-weighting, and full and local motion correction  
388 were carried out with the patch motion correction. Global and local contrast transfer function  
389 values were estimated from non-dose weighted motion-corrected images using patch CTF  
390 module. Bad micrographs with ice and ethane contamination and poor CTF fits were discarded.  
391 Subsequent image processing operations were carried out using dose-weighted, motion-  
392 corrected micrographs. 2D-class average images obtained from 1000 manually picked particles  
393 were used to pick about 2.83 and 1.04 million particles in ANP and ADP datasets. Extensive 2D-  
394 classifications of 4-8 rounds yielded 424708 and 313223 pure particles which led to 2.98 and 3.1  
395 Å consensus maps. The reported resolutions of the cryo-EM maps are based on FSC 0.143

396 criterion (35). Six-fold rotational symmetry (C6) confirmed from the 2D class averages was applied  
397 during 3D refinement. The density of ANP was confirmed at the interphase of N2D and CTD,  
398 though 2.5:1 millimolar mixture of ANP and ADP was used in the mixed nucleotide dataset. A  
399 summary of image processing of the ANP and ADP datasets can be found in Figs S1, S2,  
400 respectively.

#### 401 ***De novo* model building and structure refinement**

402 A crude model for a single BfpD subunit was built using the ADP map with *Phenix.map\_to\_model*  
403 tool (36), which was improved by chain tracing. The regions from 107-223 (N2D), 231-534 (CTD)  
404 were built. The density for the N-terminus (N1D; 1-106) and flexible linker connecting N2D and  
405 CTD (224-230) was not visualized. A clear density for a loop spanning 294-310 in the ADP  
406 structure was obtained which is disordered in the ANP structure. The monomeric model was  
407 expanded to a hexamer model. Local density fit of the modeled sequence was improved over an  
408 iterative process of amino acid fitting in Coot (37) alternated with real space refinement in PHENIX  
409 (38). Real space refinement was carried out with NCS constraints and secondary structure and  
410 Ramachandran restraints. Comprehensive model validation was carried out with PHENIX and  
411 PDB validation server at <https://validate.rcsb-2.wwpdb.org/> and are summarized in Table S1.  
412 Surface charge was calculated with chimera (39). Figures were generated with The PyMOL  
413 Molecular Graphics System, Version 2.0 Schrödinger, LLC (<https://pymol.org>) and chimera.

#### 414 **ATPase activity**

415 ATPase activity was measured using a previously established method (40, 41) with slight  
416 modifications. In brief, stocks of BfpD purified by cobalt affinity chromatography were prepared in  
417 assay buffer (150 mM Tris-HCl, pH 7.6, 300 mM NaCl, 1 mM MgCl<sub>2</sub>, 2 mM DTT) to achieve 0.5  
418 mg/ml in the final reaction and mixed with various concentrations (50 μM - 1500 μM) of freshly  
419 prepared ATP in the same assay buffer. The reaction mixtures (in triplicate) were aliquoted to 96-

420 well plates (one plate for each time point) and incubated at 37°C. At the defined time points, the  
421 reaction was stopped by adding 100 µl of the assay reagent (a 3:1 mixture of freshly prepared  
422 0.045% malachite green hydrochloride in water and 4.2% ammonium molybdate in 4 N HCl, along  
423 with 1% Triton X-100) and followed by 20 µL of citrate solution (34%). The absorbance at 655 nm  
424 was measured on a Clariostar Monochromator Microplate Reader (BMG Labtech). The ATPase  
425 activity was extrapolated from a standard curve of a set of defined phosphate concentrations  
426 present in two columns of each plate. To measure apparent  $K_m$  and  $V_{max}$ , various ATP  
427 concentrations, and the reaction was terminated at multiple time points. Released  $PO_4$   
428 concentration was plotted as a function of time for the different ATP concentrations and the slope  
429 was used as initial velocity ( $V_0$ ). Data from seven biological replicates were fit by nonlinear  
430 regression to the Michaelis-Menten equation with SigmaPlot® (Systat Software, Inc.) to calculate  
431 apparent  $K_m$  and  $V_{max}$ . The specific activity of BfpD was measured by varying BfpD concentrations  
432 (0.125 – 2.0 mg/ml) in the assay buffer (above) with 3 mM ATP and a 30 min reaction time at  
433 37°C. The rate of T4P extension in microns per time was estimated from several studies with  
434 various methods (10-12) and from an estimate of 952 T4P subunits per micron in the pilus (25).

435

436

## 437 **Appendix**

438 Supplementary material for this article is available in a separate file.

439

## 440 **Data availability**

441 Cryo-EM maps of BfpD-ANP class-1, 2 and BfpD-ADP have been deposited in the Electron  
442 Microscopy Databank (EMDB) with accession codes 27795, 27796 and 27797 respectively.

443 Atomic models of BfpD-ANP class-1, 2 and BfpD-ADP have been deposited in the RCSB PDB  
444 database with accession codes 8DZE, 8DZF, and 8DZG respectively.

#### 445 **Acknowledgments**

446 We are grateful to Kurt Piepenbrink (currently at University of Nebraska) for a providing codon-  
447 optimized BfpD construct. Cryo-grid preparation and screening were carried out at the Cryo-EM  
448 Unit at Virginia Commonwealth University (VCU), and data collection was carried out at the  
449 Molecular Electron Microscopy Core Facility at the University of Virginia (UVA) (supported by NIH  
450 U24 GM116790). We thank Dr. Kelly Dryden for cryo-EM data collection. Supported by VCU  
451 Accelerate Fund (to M.D. and M.S), NIH R56 AI111767 (to M.D.), and NIH R01 AR068431 (to  
452 M.S).

453

#### 454 **Author contributions**

455 J.L. performed protein purification and mutagenesis; P.K.S. performed enzyme assays; A.R.N.  
456 performed protein cryo-grid preparation, image processing and model building; A.R.N, M.S. and  
457 M.D. interpreted the structural data; M.D. and M.S conceived, designed and supervised all  
458 experiments, M.D., M.S., and A.N. wrote the manuscript.

459

#### 460 **Conflict of interest**

461 Authors declare that they have no conflict of interest.

462

#### 463 **References**

464

465 1. Singh PK, Little J, Donnenberg MS. 2022. Landmark Discoveries and Recent Advances in Type IV  
466 Pilus Research. *Microbiol Mol Biol Rev* doi:10.1128/mmbr.00076-22:e0007622.

467 2. Craig L, Forest KT, Maier B. 2019. Type IV pili: dynamics, biophysics and functional consequences.  
468 *Nat Rev Microbiol* 17:429-440.

469 3. Zhang HZ, Donnenberg MS. 1996. DsbA is required for stability of the type IV pilin of  
470 enteropathogenic *Escherichia coli*. *Mol Microbiol* 21:787-97.

471 4. Jakovljevic V, Leonardy S, Hoppert M, Sogaard-Andersen L. 2008. PilB and PilT are ATPases acting  
472 antagonistically in type IV pilus function in *Myxococcus xanthus*. *J Bacteriol* 190:2411-21.

473 5. Hendrick WA, Orr MW, Murray SR, Lee VT, Melville SB. 2017. Cyclic Di-GMP Binding by an  
474 Assembly ATPase (PilB2) and Control of Type IV Pilin Polymerization in the Gram-Positive  
475 Pathogen *Clostridium perfringens*. *J Bacteriol* 199.

476 6. Sakai D, Horiuchi T, Komano T. 2001. ATPase activity and multimer formation of PilQ protein are  
477 required for thin pilus biogenesis in plasmid R64. *J Biol Chem* 276:17968-75.

478 7. Chiang P, Sampaleanu LM, Ayers M, Pahuta M, Howell PL, Burrows LL. 2008. Functional role of  
479 conserved residues in the characteristic secretion NTPase motifs of the *Pseudomonas aeruginosa*  
480 type IV pilus motor proteins PilB, PilT and PilU. *Microbiology (Reading)* 154:114-126.

481 8. Kruse K, Salzer R, Joos F, Averhoff B. 2018. Functional dissection of the three N-terminal general  
482 secretory pathway domains and the Walker motifs of the traffic ATPase PilF from *Thermus*  
483 *thermophilus*. *Extremophiles* 22:461-471.

- 484 9. Sukmana A, Yang Z. 2018. The type IV pilus assembly motor PilB is a robust hexameric ATPase with  
485 complex kinetics. *Biochem J* 475:1979-1993.
- 486 10. Maier B, Koomey M, Sheetz MP. 2004. A force-dependent switch reverses type IV pilus retraction.  
487 *Proc Natl Acad Sci U S A* 101:10961-6.
- 488 11. Skerker JM, Berg HC. 2001. Direct observation of extension and retraction of type IV pili. *Proc Natl*  
489 *Acad Sci U S A* 98:6901-4.
- 490 12. Ellison CK, Dalia TN, Vidal Ceballos A, Wang JC, Biais N, Brun YV, Dalia AB. 2018. Retraction of DNA-  
491 bound type IV competence pili initiates DNA uptake during natural transformation in *Vibrio*  
492 *cholerae*. *Nat Microbiol* 3:773-780.
- 493 13. Clausen M, Koomey M, Maier B. 2009. Dynamics of type IV pili is controlled by switching between  
494 multiple states. *Biophys J* 96:1169-77.
- 495 14. McCallum M, Tammam S, Khan A, Burrows LL, Howell PL. 2017. The molecular mechanism of the  
496 type IVa pilus motors. *Nat Commun* 8:15091.
- 497 15. Mancl JM, Black WP, Robinson H, Yang Z, Schubot FD. 2016. Crystal Structure of a Type IV Pilus  
498 Assembly ATPase: Insights into the Molecular Mechanism of PilB from *Thermus thermophilus*.  
499 *Structure* 24:1886-1897.
- 500 16. Collins R, Karupiah V, Siebert CA, Dajani R, Thistlethwaite A, Derrick JP. 2018. Structural cycle of  
501 the *Thermus thermophilus* PilF ATPase: the powering of type IVa pilus assembly. *Sci Rep* 8:14022.
- 502 17. Solanki V, Kapoor S, Thakur KG. 2018. Structural insights into the mechanism of Type IVa pilus  
503 extension and retraction ATPase motors. *FEBS J* 285:3402-3421.

- 504 18. Jessop M, Arragain B, Miras R, Fraudeau A, Huard K, Bacia-Verloop M, Catty P, Felix J, Malet H,  
505 Gutsche I. 2020. Structural insights into ATP hydrolysis by the MoxR ATPase RavA and the Ldcl-  
506 RavA cage-like complex. *Commun Biol* 3:46.
- 507 19. Landsberg MJ, Vajjhala PR, Rothnagel R, Munn AL, Hankamer B. 2009. Three-dimensional  
508 structure of AAA ATPase Vps4: advancing structural insights into the mechanisms of endosomal  
509 sorting and enveloped virus budding. *Structure* 17:427-37.
- 510 20. Zhang X, Shaw A, Bates PA, Newman RH, Gowen B, Orlova E, Gorman MA, Kondo H, Dokurno P,  
511 Lally J, Leonard G, Meyer H, van Heel M, Freemont PS. 2000. Structure of the AAA ATPase p97.  
512 *Mol Cell* 6:1473-84.
- 513 21. Stone KD, Zhang HZ, Carlson LK, Donnenberg MS. 1996. A cluster of fourteen genes from  
514 enteropathogenic *Escherichia coli* is sufficient for the biogenesis of a type IV pilus. *Mol Microbiol*  
515 20:325-37.
- 516 22. Priess M, Goddeke H, Groenhof G, Schafer LV. 2018. Molecular Mechanism of ATP Hydrolysis in  
517 an ABC Transporter. *ACS Cent Sci* 4:1334-1343.
- 518 23. Abendroth J, Murphy P, Sandkvist M, Bagdasarian M, Hol WG. 2005. The X-ray structure of the  
519 type II secretion system complex formed by the N-terminal domain of EpsE and the cytoplasmic  
520 domain of EpsL of *Vibrio cholerae*. *J Mol Biol* 348:845-55.
- 521 24. Karupiah V, Collins RF, Thistlethwaite A, Gao Y, Derrick JP. 2013. Structure and assembly of an  
522 inner membrane platform for initiation of type IV pilus biogenesis. *Proc Natl Acad Sci U S A*  
523 110:E4638-47.

- 524 25. Craig L, Volkmann N, Arvai AS, Pique ME, Yeager M, Egelman EH, Tainer JA. 2006. Type IV pilus  
525 structure by cryo-electron microscopy and crystallography: implications for pilus assembly and  
526 functions. *Mol Cell* 23:651-62.
- 527 26. Camberg JL, Johnson TL, Patrick M, Abendroth J, Hol WG, Sandkvist M. 2007. Synergistic  
528 stimulation of EpsE ATP hydrolysis by EpsL and acidic phospholipids. *EMBO J* 26:19-27.
- 529 27. Lu C, Turley S, Marionni ST, Park YJ, Lee KK, Patrick M, Shah R, Sandkvist M, Bush MF, Hol WG.  
530 2013. Hexamers of the type II secretion ATPase GspE from *Vibrio cholerae* with increased ATPase  
531 activity. *Structure* 21:1707-17.
- 532 28. Li C, Wen A, Shen B, Lu J, Huang Y, Chang Y. 2011. FastCloning: a highly simplified, purification-  
533 free, sequence- and ligation-independent PCR cloning method. *BMC Biotechnol* 11:92.
- 534 29. Wang RF, Kushner SR. 1991. Construction of versatile low-copy-number vectors for cloning,  
535 sequencing and gene expression in *Escherichia coli*. *Gene* 100:195-9.
- 536 30. Crowther LJ, Anantha RP, Sonnenberg MS. 2004. The inner membrane subassembly of the  
537 enteropathogenic *Escherichia coli* bundle-forming pilus machine. *Molecular Microbiology* 52:67-  
538 79.
- 539 31. Higuchi R, Krummel B, Saiki RK. 1988. A general method of in vitro preparation and specific  
540 mutagenesis of DNA fragments: study of protein and DNA interactions. *Nucleic Acids Res* 16:7351-  
541 67.
- 542 32. Ohi M, Li Y, Cheng Y, Walz T. 2004. Negative Staining and Image Classification - Powerful Tools in  
543 Modern Electron Microscopy. *Biol Proced Online* 6:23-34.



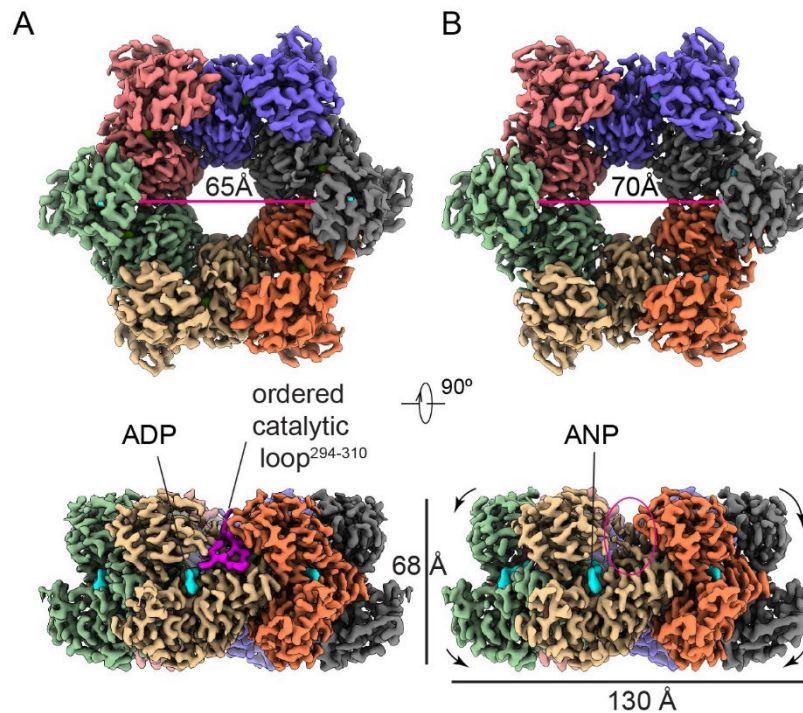
- 544 33. Shaikh TR, Gao H, Baxter WT, Asturias FJ, Boisset N, Leith A, Frank J. 2008. SPIDER image  
545 processing for single-particle reconstruction of biological macromolecules from electron  
546 micrographs. *Nat Protoc* 3:1941-74.
- 547 34. Passmore LA, Russo CJ. 2016. Specimen Preparation for High-Resolution Cryo-EM. *Methods*  
548 *Enzymol* 579:51-86.
- 549 35. Scheres SH, Chen S. 2012. Prevention of overfitting in cryo-EM structure determination. *Nat*  
550 *Methods* 9:853-4.
- 551 36. Terwilliger TC, Adams PD, Afonine PV, Sobolev OV. 2018. A fully automatic method yielding initial  
552 models from high-resolution cryo-electron microscopy maps. *Nat Methods* 15:905-908.
- 553 37. Emsley P, Lohkamp B, Scott WG, Cowtan K. 2010. Features and development of Coot. *Acta*  
554 *Crystallogr D Biol Crystallogr* 66:486-501.
- 555 38. Afonine PV, Poon BK, Read RJ, Sobolev OV, Terwilliger TC, Urzhumtsev A, Adams PD. 2018. Real-  
556 space refinement in PHENIX for cryo-EM and crystallography. *Acta Crystallogr D Struct Biol*  
557 74:531-544.
- 558 39. Pettersen EF, Goddard TD, Huang CC, Couch GS, Greenblatt DM, Meng EC, Ferrin TE. 2004. UCSF  
559 Chimera--a visualization system for exploratory research and analysis. *J Comput Chem* 25:1605-  
560 12.
- 561 40. Lanzetta PA, Alvarez LJ, Reinach PS, Candia OA. 1979. An improved assay for nanomole amounts  
562 of inorganic phosphate. *Anal Biochem* 100:95-7.

563 41. Yamagata A, Milgotina E, Scanlon K, Craig L, Tainer JA, Donnenberg MS. 2012. Structure of an  
564 essential type IV pilus biogenesis protein provides insights into pilus and type II secretion systems.  
565 J Mol Biol 419:110-24.

566

567

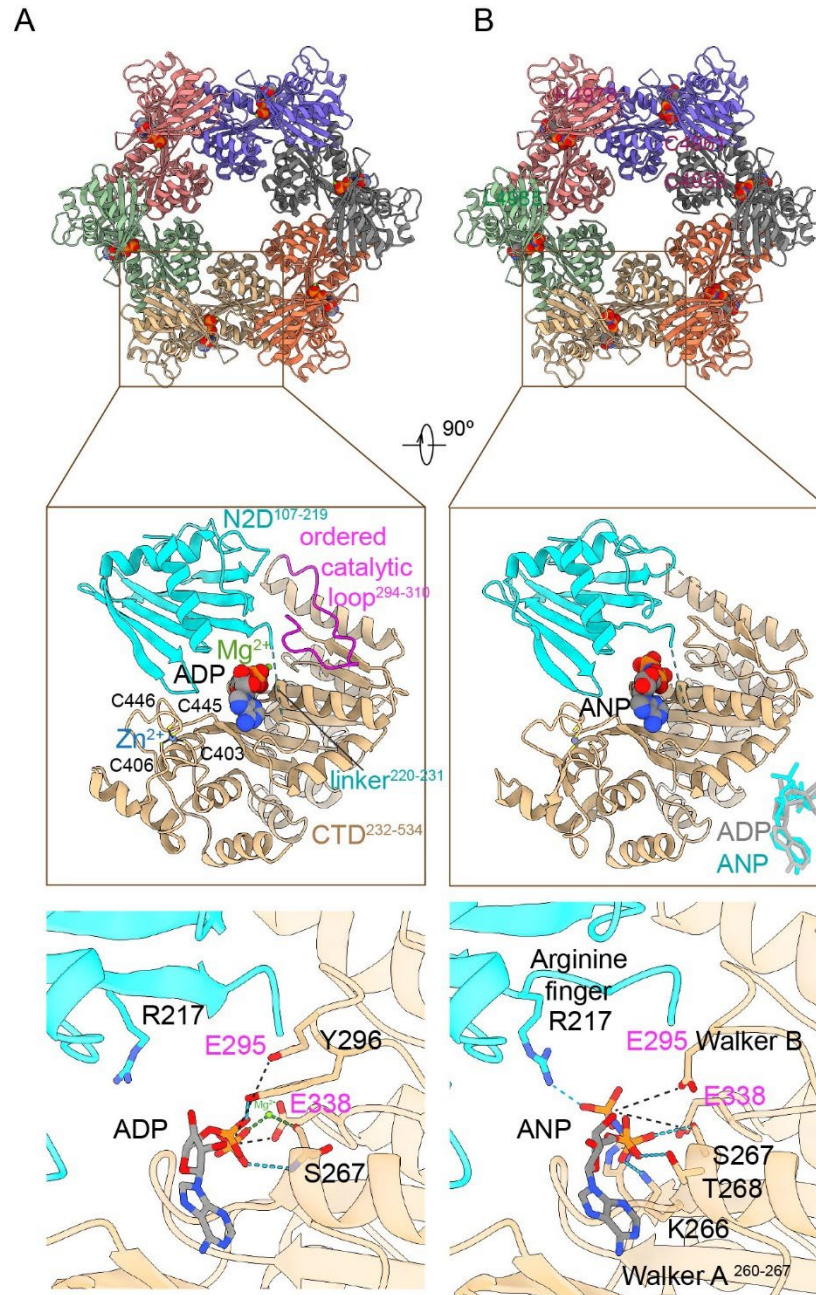
568 **Figures**



569

570 **Figure 1.** Cryo-EM maps of six-fold symmetric BfpD and its nucleotide binding pocket. 3D  
571 reconstruction of BfpD in (A) ADP and (B) a mixture of ADP, ATP, and ANP resolved at 3.0 Å and  
572 3.1 Å resolution shown in two orthogonal orientations. Top row, view N2D facing the viewer.  
573 Bottom row, side view with N2D at the top. The diameter of BfpD toroid center expands by ~5 Å  
574 (arrows) in the presence of ANP compared to the diphosphate. Each subunit is colored differently,  
575 and the nucleotide is represented in cyan. The EM density for the loop harboring catalytic Glu295  
576 (magenta) is well defined in the ADP structure, but not in the ANP structure (red oval).

577

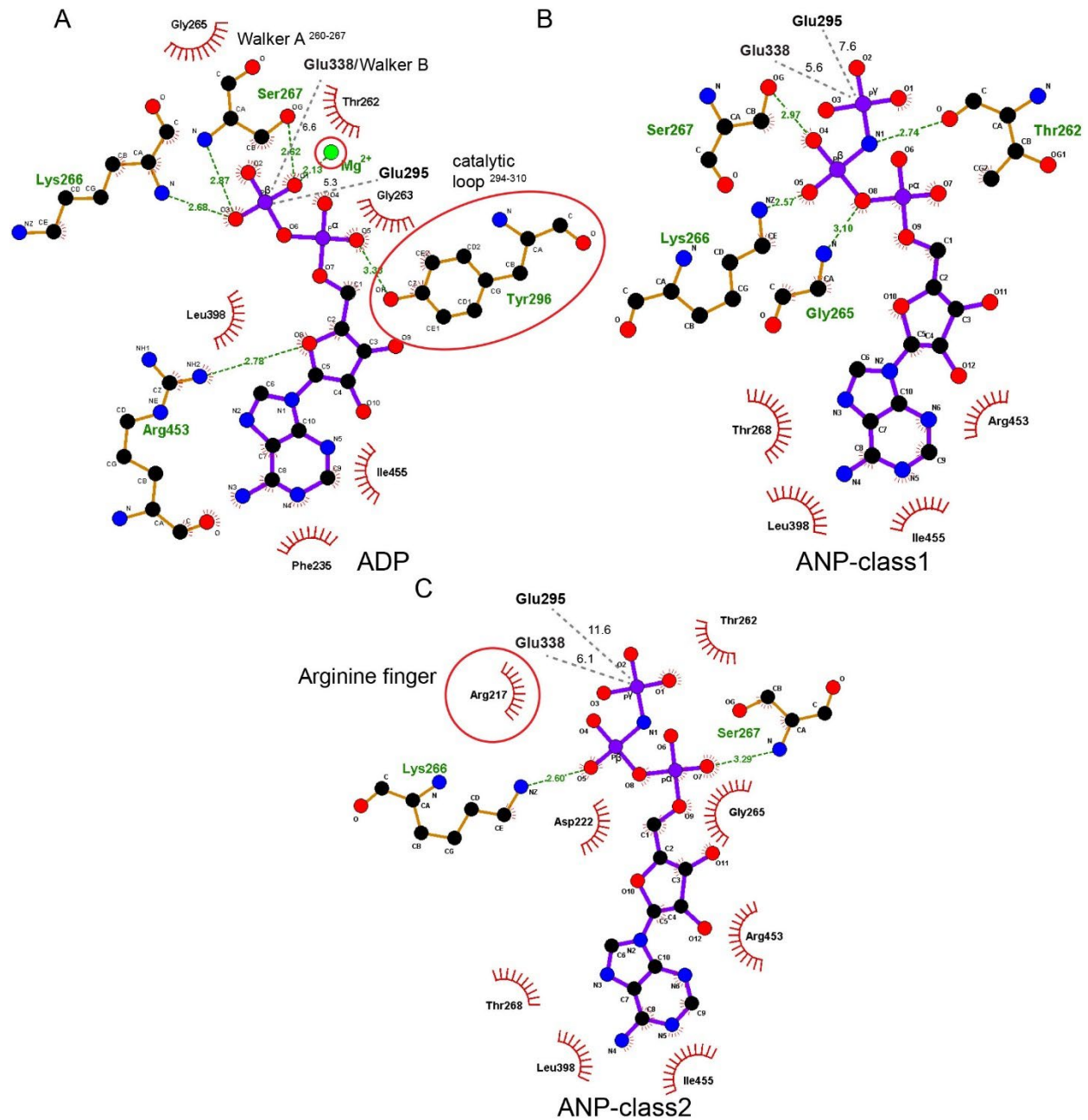


578

579 **Figure 2.** *De novo* models of BfpD-ADP (A) and BfpD-ANP (B). In the upper panel, each monomer  
580 is represented in a different color. The middle panel shows the domain organization of one subunit  
581 with the nucleotide, Mg<sup>2+</sup>, ordered catalytic loop and tetracysteine motif shown in BfpD-ADP. Key  
582 amino acids at the N2D-CTD domain interface responsible for nucleotide binding (black) and  
583 hydrolysis (magenta) are shown in the lower panel. The catalytic Glu295 and Walker B Glu338

584 are positioned at 5.3-11.6 and ~6 Å in ADP and ANP models respectively. In the BfpD-ANP model,  
585 an interaction between the  $\gamma$ -phosphate and Arg217 repositions the loop carrying the catalytic  
586 Glu295.

587



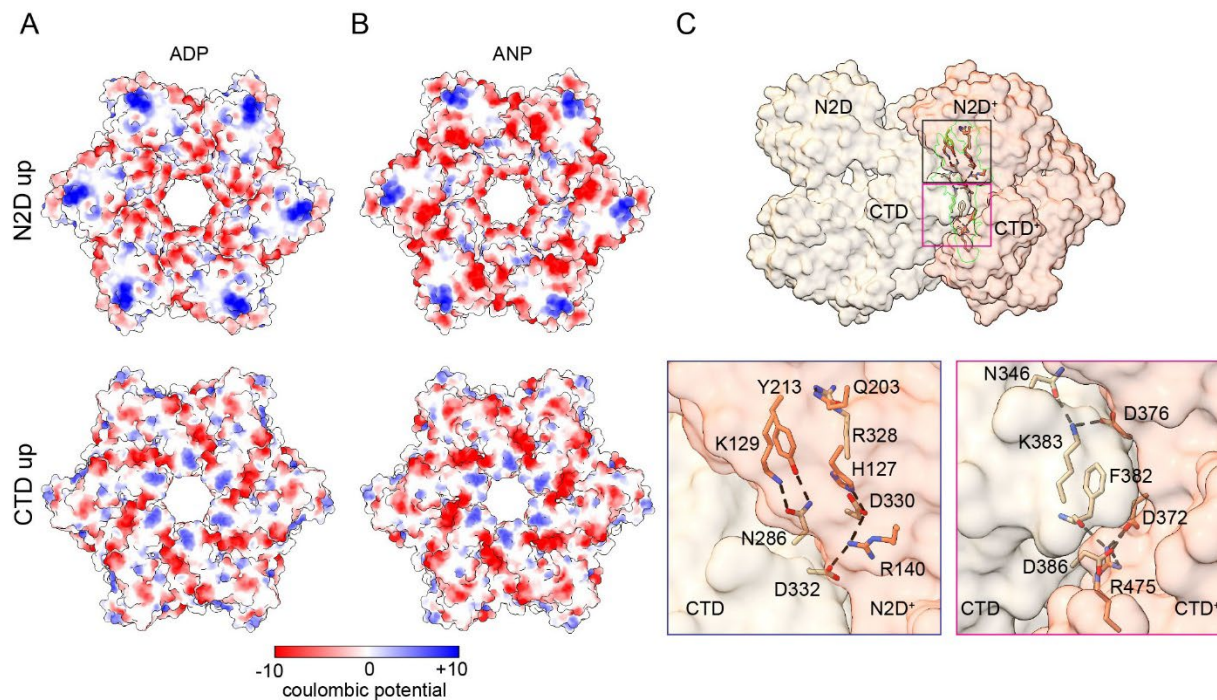
588

589 **Figure 3.** BfpD active site reorganization upon ATP hydrolysis. 2D representation of the BfpD  
590 catalytic site in (A) BfpD-ADP, (B) BfpD-ANP-class1, and (C) BfpD-ANP-class2 structures. The  
591 detail shows changes in the interaction network associated with the conformational change that  
592 occurs upon transition from dinucleotide to trinucleotide bound. Arg217 repositions to stabilize  
593 and place the  $\gamma$ -phosphate of ANP at a farther distance from Glu295. Hydrogen bonds, in Å, are

594 shown with green dashed lines, non-bonded interactions are shown by red arcs. Tyr296 and  
595 Arg217 are highlighted to emphasize their important role in the indicated conformations.

596



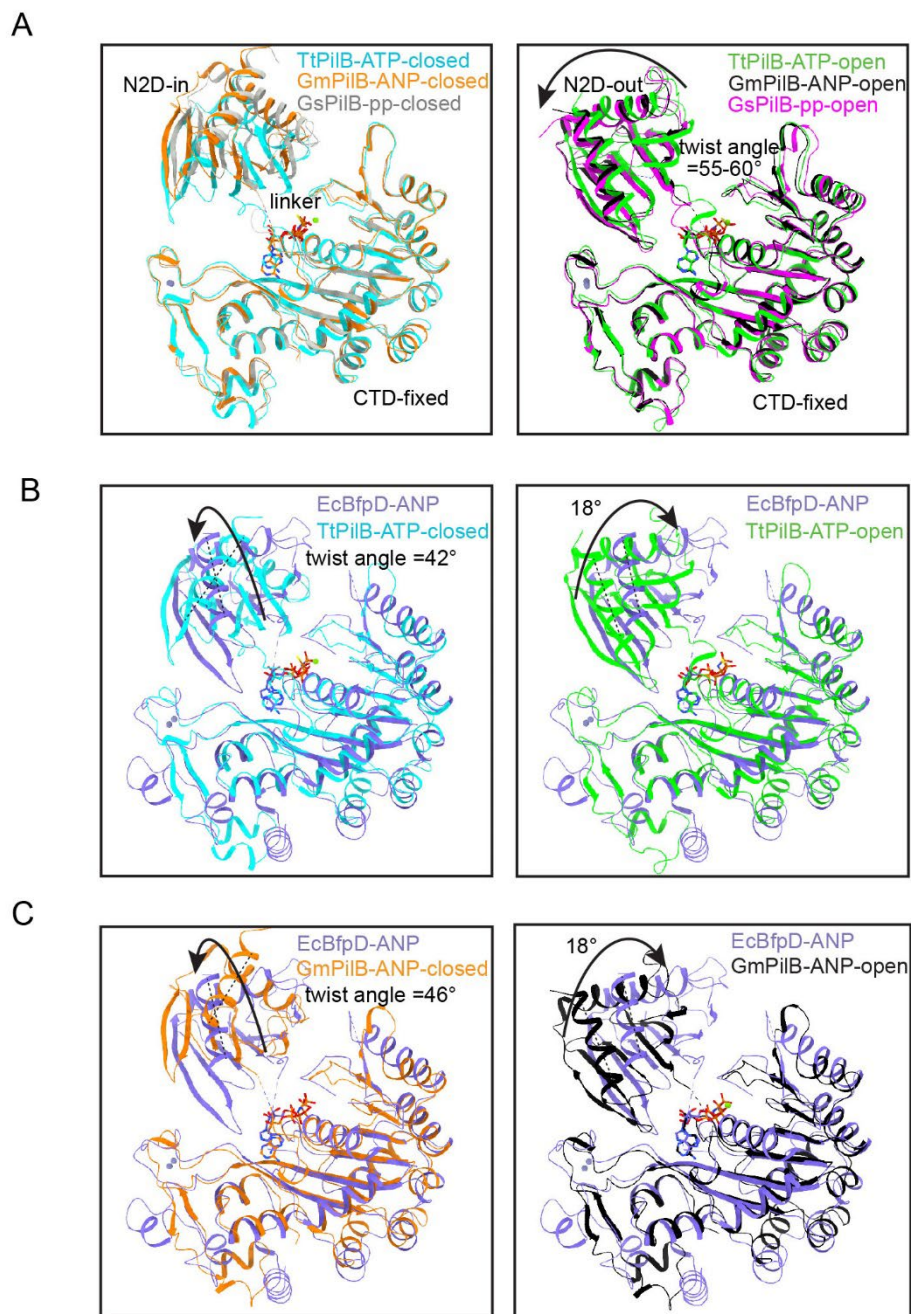


597

598 **Figure 4.** Charge distribution and interacting surfaces of BfpD. Surface electrostatics  
599 representation for BfpD-ADP (A) and BfpD-ANP (B). Top, the N2D facing surface of BfpD that  
600 has clusters of positively charged residues (in blue), suggesting this side most likely faces the  
601 plasma membrane. Bottom, CTD facing surface showing overall negatively charged residues (in  
602 red). (C) Top, side view of two neighboring BfpD subunits with the interacting space highlighted  
603 (green). Bottom, the CTD of the left subunit (tan) interacts with the N2D+ and CTD+ of the subunit  
604 (salmon) on the right. Salt bridges and hydrogen bonds <math><3.7 \text{ \AA}</math> are shown.

605

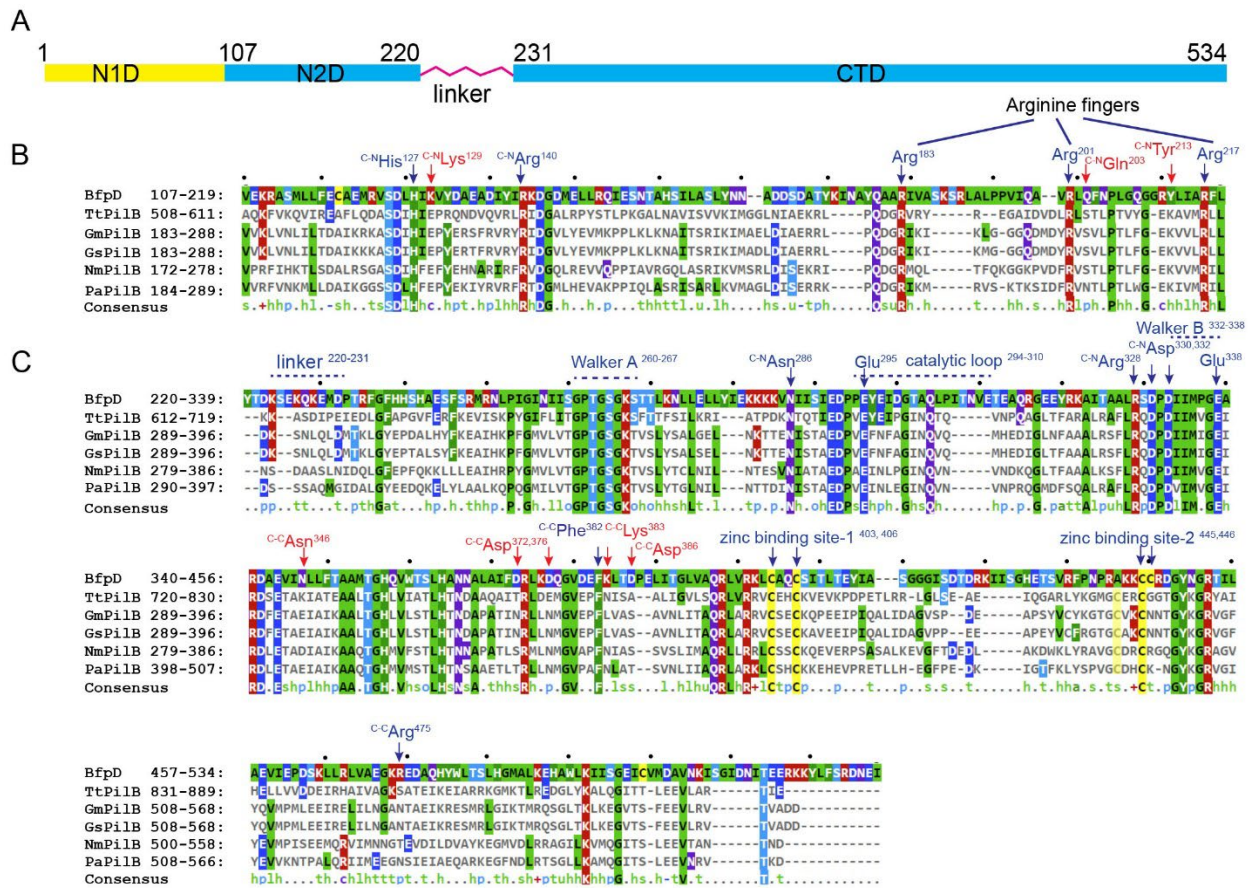




607 **Figure 5.** The N-terminal domain of BfpD has a distinct twist and rotation axis. (A) Two distinct  
608 conformations of pilus extension ATPase subunits were found in two-fold symmetric TtPilB,  
609 GmPilB, and GsPilB bound to ATP, AMP-PNP (ANP), and phosphate (pp) respectively. In A, the  
610 closed, left, and open, right, subunits are overlaid, keeping the CTDs fixed. The arrow shows  
611 rotation in N2D from closed to open conformation in each structure. In (B) and (C), the N2D

612 domain of enteropathogenic *E. coli* BfpD is compared with the TtPilB-ATP and GmPilB-ANP  
 613 structures, respectively. The arrow in the left indicates transition from closed TtPilB-ATP or  
 614 GmPilB-ANP to BfpD-ANP. The arrow in the right indicates transition from TtPilB-ATP-open to  
 615 BfpD-ANP. For the two-fold structures, the comparisons between BfpD and “open” are shown for  
 616 the more extreme open (N2D-out) conformation; see Fig. S4.

617

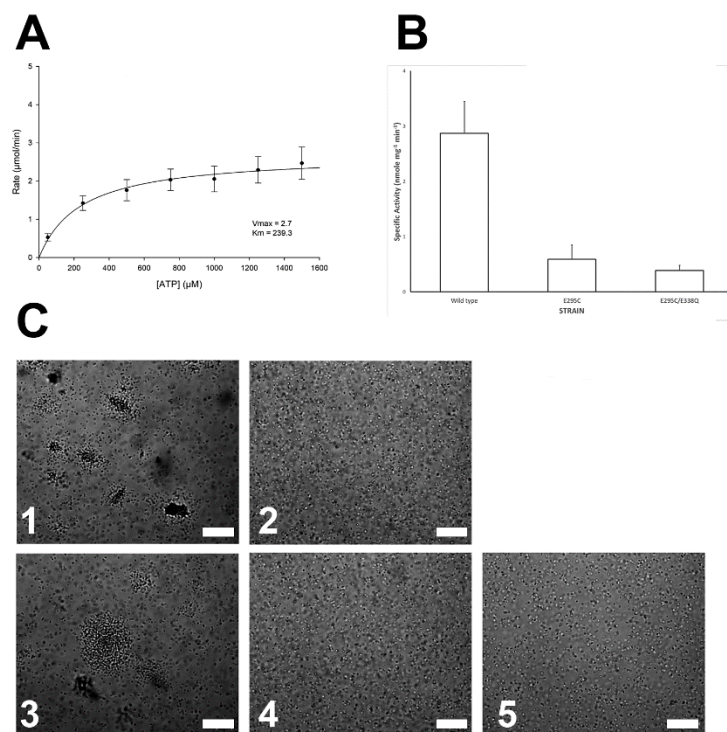


618

619 **Figure 6.** Sequence comparisons of T4P extension ATPase N2D and CTD domains and inter-  
 620 subunit contacts in BfpD. The alignment of BfpD with five homologues is shown. TtPilB, GmPilB,  
 621 and GsPilB form two-fold symmetric hexamers and PilB from *P. aeruginosa* and *N. meningitidis*  
 622 are members of the type-4 pilus ATPases more closely related to them than to BfpD. (A) Domain

623 organization. (B) alignment of the N2D domains shows insertions in BfpD between three  
624 conserved Arginine fingers relative to the other enzymes. (C) alignment of the CTD domains  
625 shows insertions in the linker region and in the catalytic loop. Sequence elements required for  
626 nucleotide binding (Walker A), hydrolysis (Glu295, Glu338) and zinc binding are highlighted.  
627 Amino acids forming inter-subunit contacts between CTD and N2D/CTD<sup>+</sup> of neighboring subunits  
628 are indicated, with text specifying the partner contact. Interactions unique to BfpD are colored  
629 red.

630



631

632 **Figure 7.** Specific activity, kinetics, and function of BfpD. (A) Rate of inorganic phosphate  
633 production as a function of the concentration of ATP for wild type BfpD, from which the apparent  
634  $K_m$  and  $V_{max}$  were calculated using Sigma Plot software. Data are from seven biological replicates.  
635 (B) Specific activity of BfpD with native (wild type), cysteine substituted for glutamate 295 (single  
636 mutant), and both E295C and E338Q substitutions (double mutant). The mean and standard error  
637 of the means of seven biological replicates is shown. Analysis of variance revealed significant  
638 differences ( $P < 0.001$ ) between groups. (C) phase-contrast micrographs of (1) wild type, (2) *bfpD*  
639 mutant, and *bfpD* mutant strains complemented with plasmids encoding (3) wild type BfpD, (4)  
640 BfpD<sub>E295C</sub>, and (5) BfpD<sub>E338Q</sub>. Large aggregates of bacteria indicative of BFP expression are seen  
641 in panels 1 and 3. Bars indicate 40 microns.

642

643